

Combined holographic-mechanical optical tweezers: Construction, optimisation and calibration

Richard D.L. Hanes, Matthew C. Jenkins, Stefan U. Egelhaaf
Condensed Matter Physics Laboratory,
Heinrich-Heine University, 40225 Düsseldorf, Germany

November 4, 2018

Abstract

We have combined a spatial light modulator (SLM) and galvanometer-mounted mirrors into an optical tweezers set-up. This provides great flexibility by allowing us to create an array of traps which can be moved in a smooth and fast way. To optimise the performance we investigated the effect of incidence angle on the SLM with respect to phase and intensity response. Although it is possible to use the SLM at an incidence of 45 degrees, smaller angles give a more constant response with a full 2π phase shift. We calibrate the traps using an active oscillatory technique and a passive probability distribution technique.

1 Introduction

Since the invention of optical tweezers, they have had a major impact on the way nanoparticles can be manipulated, especially in biology and colloidal physics. The first realisation was shown by Ashkin in 1970 [1] where he demonstrated that spheres in a solvent of lower refractive index are drawn into a laser beam, as well as being accelerated along it. He later went on to show that a tightly focused beam can create a stable trap in three dimensions [2], giving rise to the modern day optical tweezers [3, 4, 5, 6]. Mirrors mounted on galvanometers can be used to steer the laser beam and hence move the trap within the sample. Even multiple trap tweezers have been realised which split one beam into multiple traps in two or three dimensions using phase holograms [7, 8, 9, 10, 11, 12] or acousto-optic modulators [13, 14, 15]. All

these techniques allow for motion of the traps, with associated advantages and disadvantages for each [3, 16]. In addition to manipulation i.e. exerting a force on particles, tweezers can also be used to measure forces in the pico- and femtonewton range [17, 18, 19].

This paper discusses a specific implementation of optical tweezers which combines a spatial light modulator (SLM) with galvanometer-mounted mirrors. The SLM can generate complex arrays of traps in three dimensions, but the trap dynamics are limited by the refresh rate of the device. The galvanometer-mounted mirrors can translate the trap array in a fast and continuous way, increasing the flexibility compared to an SLM alone. Furthermore, by using both devices together we can calibrate multiple traps simultaneously, allowing the traps to then be used for force measurements.

2 Optical tweezers set-up

A schematic representation of the set-up is shown in fig 1. We use a DPSS 532 nm 1.5 W CW laser (Laser Quantum Ventus 532-1500). The polarisation angle is rotated by a half-wave plate ($\lambda/2$), necessary for the SLM later in the optical path. The beam is reflected from mirror M1 (all mirrors from Thorlabs), then passes through a 10x beam expander BE (Newport NT55-578), which takes it from 1.4 mm to 14 mm, the length of the longest edge of the SLM. It strikes the SLM (Holoeye LCR-2500) at 22.5° angle of incidence and passes through the analyser A which, together with the half-wave plate, is necessary to optimise the de-

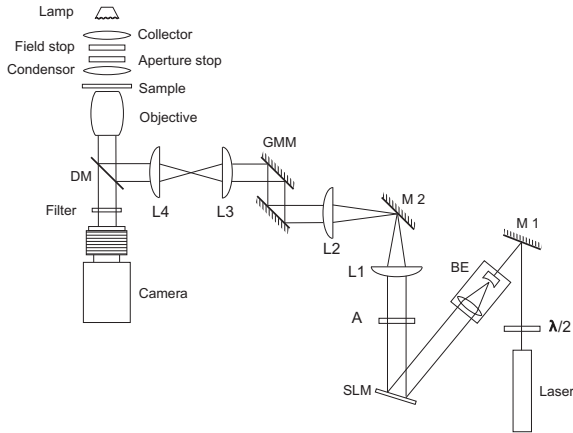


Figure 1: Schematic diagram of the setup combining galvanometer-mounted mirrors (GMM) and a spatial light modulator (SLM) into optical tweezers (see text for details).

vice performance (sec 4). The light from the SLM is then imaged onto the galvanometer mounted mirrors GMM (Nutfield Technology Inc. Quantum Scan 30) by a telescope formed by lenses L1 ($f_1=175$ mm planoconvex, all lenses from Edmund Optics) and L2 ($f_2=100$ mm planoconvex) which also reduces the diameter from 14 mm to 8 mm. Between the two lenses it is reflected vertically by mirror M2, to align the beam with the microscope epifluorescence port. The GMM consists of an X-Y frame (XLR8 Open-frame head QS30, Nutfield Technology Inc.) and two galvanometer-mounted mirrors for in-plane trap translation. From here, the beam traverses the second telescope formed by lenses L3 ($f_3=125$ mm planoconvex) and L4 ($f_4=100$ mm planoconvex) which reduces the beam to its final diameter of 6.4 mm, to slightly overfill the back aperture of the microscope objective. Combined imaging and trapping is facilitated by a dichroic mirror DM (transmission in the range 525-540 nm is lower than 0.12, z532dcrb Chroma Technology Corp.) which reflects the laser light into a 1.4 NA 100x Nikon objective. For imaging we use an inverted microscope (Nikon TE2000-U). The intense laser light is separated from the imaging light by a filter (notch filter, transmission in the range 525-538 nm is lower than 10^{-6} , z532nf Chroma Technology Corp.). The filter, the dichroic mirror DM and the lens L4 are housed within a home-built

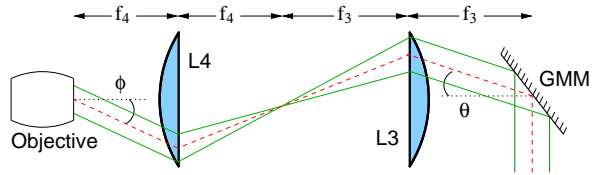


Figure 2: The rotation angle θ_{GMM} of the galvanometer mounted mirrors results in a tilt θ_{Obj} at the back aperture of the objective. It is constrained by the geometry of the setup. Note that the GMM consists of two mirrors; only one is shown for clarity.

filter cube within the microscope. For capturing images we use a Pixelink PL-B742F CMOS camera controlled by LabView (National Instruments).

3 Galvanometer construction

We use two galvanometer-mounted mirrors GMM to steer the beam into lens L3, part of the final telescope in the system (fig 2). The telescope images the mirrors onto the back aperture of the objective, so a rotation of the mirrors by an angle θ_{GMM} corresponds to a rotation of the beam at the aperture through an angle θ_{Obj} , and an in-plane translation of the trap(s). The geometry of the second telescope gives rise to a natural maximum mirror rotation angle θ_{GMM}^{max} and hence a maximum translation distance within the sample.

The distance between the central point between the two galvanometer mounted mirrors and lens L3 is $f_3=125$ mm. (The misalignment resulting from the distance between the two mirrors is small enough to be effectively ignored.) The diameter of lens L3 is 25.4 mm and the beam diameter at this point 8 mm, giving a maximum displacement across the surface of lens L3 of $(25.4 \text{ mm} - 8 \text{ mm})/2 = 8.7$ mm and a maximum rotation angle $\theta_{GMM}^{max} = \tan^{-1}(8.7 \text{ mm}/125 \text{ mm}) = 3.98^\circ$. The GMM is controlled by a digital-to-analogue card DA (National Instruments PCI-6014) and home-written LabView software. The output range from the DA is -10 V to +10 V (with smallest step 5.8 mV) corresponding to a maximum rotation range of the mirrors of $\pm 48^\circ$ with increment 0.03° . Since we are using a small range of angles $|\theta_{GMM}| < \theta_{GMM}^{max}$ we incorporated a 10x voltage divider between the com-

puter and galvanometer control electronics (Quantum Drive 3000) resulting in a maximum rotation of the mirrors of $\pm 4.8^\circ$ with increment 0.003° . At the objective this corresponds to a maximum angular rotation of $\theta_{Obj}^{max} = 5.42^\circ$ and an in-plane displacement of $\pm 83 \mu\text{m}$ (determined experimentally). The time taken for one galvanometer to move through a step of 0.5° (equal to $10.6 \mu\text{m}$ in-plane translation) and settle to within 90% of its final position is 0.65 ms (manufacturer's specifications). With the SLM this speed is possible, but not smoothly, due to its limited refresh rate (72 Hz).

The lateral displacement of the trap was experimentally determined and calibrated as follows. The filter was removed from the imaging path and the lowest available laser power used. This allowed us to observe the reflection of the beam from the interface between the cover slip and the solvent. This was quantitatively tracked using a custom-written LabView routine. By moving a trap in the x and y directions the GMM voltage could be related to the lateral displacement in pixels. No significant differences were found for different positions within the field of view. The pixels were then related to absolute measures from the image of a Richardson test slide. This procedure yielded the above stated maximum in-plane translation range of $\pm 83 \mu\text{m}$.

4 SLM characterisation

To optimise the performance of the tweezers system the SLM was characterised in detail. This includes the size and shape of each trap as well as the relative intensities of the desired first order projections relative to the zero and higher order (ghost) traps. An SLM working at optimum efficiency (ignoring for the moment the algorithm used to calculate the phase holograms [20]) will be able to modify the phase of the incoming light by 2π , without significantly affecting its amplitude. A SLM uses nematic liquid crystals to control the refractive index at each pixel, making it highly sensitive to the incoming polarisation orientation. It also causes a slight depolarisation which reduces the efficiency, and requires an analyser to define the polarisation.

We use a Holoeye LCR-2500 SLM which gives a 2π phase shift from 400 nm to 700 nm when illuminated with a small angle of incidence (manufacturer's specifications). We used home-written

LabView software for the characterisation procedure. For this device we investigated experimentally the effects of changing the incidence angle α and wavelength λ on the output intensity and phase. The different incidence angles require interferometers with different geometries (fig 3). The set-up used for zero angle incidence geometry represents a Michelson-Morley interferometer [21] (fig 3a). The beam is first expanded by a beam expander BE and then split by a beam splitter cube BS (B.Halle, TWK-20) between a mirror M and the SLM. The reflections are collected at the same cube BS, passed through an analyser A and recorded on the camera. The incoming beam polarisation is rotated using a half wave plate ($\lambda/2$). For incidence angles $\alpha \leq 22.5^\circ$ we used another interferometer (fig 3b). This set-up contains two beam splitter cubes, BE1 to divide the incoming beam and the BE2 to recombine them. The symmetry of the set-up with about equal path length is important, as the coherence length of our laser is only about 1 cm. A similar set-up, but with rectangular geometry, a Mach-Zehnder interferometer [22, 23], is applied for an incidence angle $\alpha = 45^\circ$ (fig 3c).

4.1 Output intensity

In our set-up, we want the SLM to introduce a phase shift $\Delta\phi$ without affecting the intensity. To find the optimum configuration we characterised the SLM. For different incidence angles α , we determined the output intensity as a function of the polarisations of the incident and reflected beams and the phase shift at the SLM. This was done as follows. We blocked the mirror arm of the set-up using a beam dump, and recorded the intensity I reflected from the SLM using the camera. The intensity recorded across all pixels of the camera was averaged. It was ensured that when the laser was off the camera recorded zero background intensity and that saturation of the camera was avoided. The input, φ_i , and output, φ_r , polarisations are selected using the half-wave plate ($\lambda/2$) and analyser A. The polarisations are defined relative to the lab vertical and increase clockwise in the direction of beam propagation. The phase shift $\Delta\phi$ introduced by the SLM is then increased in steps and the intensity I measured. We used an increment of 1 out of the 256 levels that our SLM offers, i.e. $0 \leq N_{\Delta\phi} < 256$. An example of the dependence of the intensity

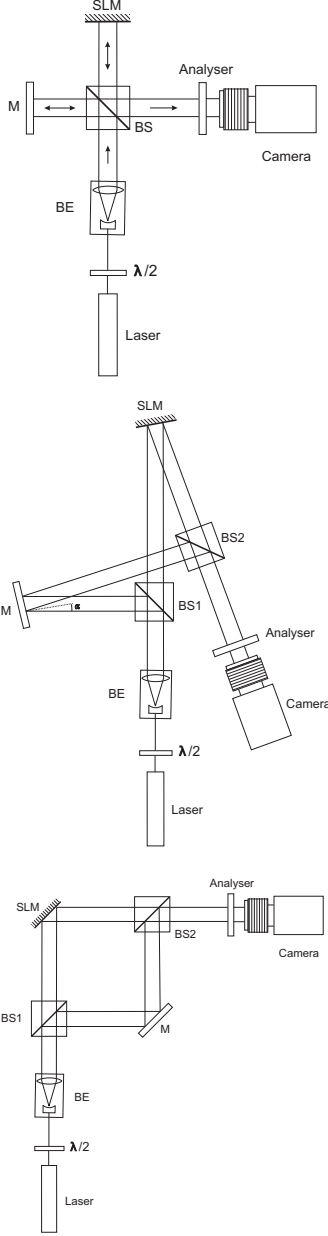


Figure 3: Interferometric set-ups used for determining the intensity and phase maps at different incidence angles α . (a) $\alpha = 0^\circ$, (b) $3^\circ < \alpha \leq 22.5^\circ$ and (c) $\alpha = 45^\circ$. For the intensity measurements, the beam directed towards the mirror M is covered and the camera used as a power meter. (See text for details.)

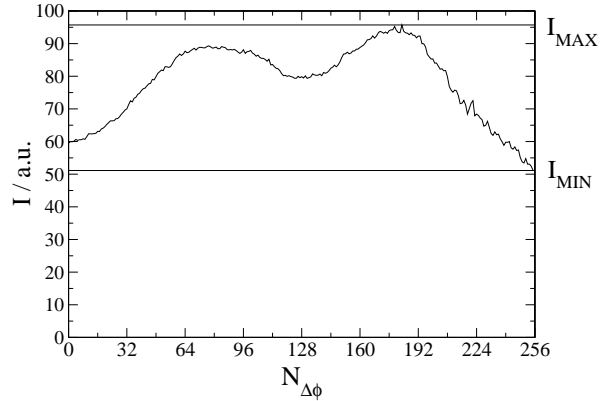


Figure 4: Output intensity I as a function of phase shift $N_{\Delta\phi}$ introduced by the SLM for an incident angle $\alpha = 22.5^\circ$ and input and output polarization $\varphi_i = 140^\circ$ and $\varphi_o = 0^\circ$ respectively.

on the phase shift is shown in fig 4.

As a measure of the flatness of the response, we use the ratio between minimum and maximum value I_{MIN}/I_{MAX} , therefore values close to one indicate an output intensity I almost independent of the phase shift $\Delta\phi$. (Note that in other literature [24] the output amplitude A is considered with $I_{MIN}/I_{MAX} = (A_{MIN}/A_{MAX})^2$.) The dependence of this ratio on φ_i and φ_o is shown in fig 5 for different incidence angles α . We covered a range $0^\circ \leq \varphi_{i,o} \leq 180^\circ$ in increments of 20° with the results at $\varphi_{i,o} = 0^\circ$ and $\varphi_{i,o} = 180^\circ$ being identical within experimental uncertainties.

The intensity maps (fig 5) show that there are clear plateaus with I_{MIN}/I_{MAX} close to 1 for all values of α . However, we also require $\Delta\phi \geq 2\pi$, which is shown in sec 4.2 not to be satisfied for most of these maxima. The $\alpha = 0^\circ$ configuration transmits only a quarter of the laser intensity into the tweezers and was therefore rejected. The $\alpha = 4^\circ$ configuration was rejected due to space requirements and to avoid long beam paths with their sensitivity to vibrations. The map for $\lambda = 633$ nm (fig 5) shows that I_{MIN}/I_{MAX} is dependent on λ , therefore re-calibration is necessary if λ is changed.

4.2 Phase change

We now relate $N_{\Delta\phi}$ to the actual phase shift $\Delta\phi$ and determine the maximum phase shift accessible for the different parameters; φ_i , φ_o , α and λ . The

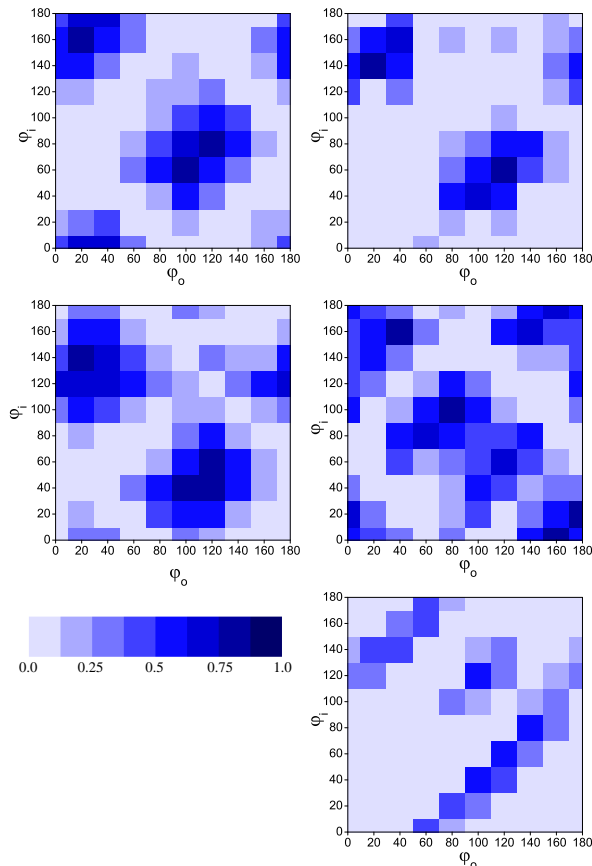


Figure 5: Ratio between minimum and maximum intensity I_{MIN}/I_{MAX} as a function of input, φ_i , and output, φ_o , polarisation for different incident angles $\alpha = 0^\circ, 4^\circ, 22.5^\circ$ and 45° (top left, top right, middle left, middle right respectively). In the lower right figure $\alpha = 45^\circ$ and $\lambda=633$ nm; in all other figures $\lambda=532$ nm.

same set-ups are used (fig 3) but with the beam dump removed from the mirror arm of the interferometer. The mirror was aligned to produce vertical fringes with a fringe width of 64 pixels, which was shown to provide optimum conditions considering processing errors and statistics due to the number of detectable fringes [24]. The two halves (top and bottom) of the SLM are programmed separately, one being held at a constant $N_{\Delta\phi}=0$, the other increased in steps of 1. As the difference in $N_{\Delta\phi}$ and hence the optical path length between the two halves of the SLM increases, the fringes on the two halves shift relative to each other. To recover the phase shift $\Delta\phi$, we took cross-sections from the top and bottom of the image. By cross-correlating these two signals, and finding the first maximum, we recover the shift in pixels. This is converted to actual phase shift $\Delta\phi$ by dividing by the period of the fringes in pixels, found from the Fourier transform of one of the signals.

We investigated the maximum accessible range of the phase shift for incident angles $\alpha = 22.5^\circ$ and $\alpha = 45^\circ$ for the same range of input, φ_i , and output, φ_o , polarisations as above, i.e. $0^\circ \leq \varphi_{i,o} \leq 180^\circ$ in increments of 20° (fig 6) Close to the optimum conditions, we used increments of 1° (data not shown). We found that, for $\alpha = 45^\circ$, there was no configuration which gave a full 2π phase shift with $I_{MIN}/I_{MAX} > 0.1$. Therefore we use the $\alpha = 22.5^\circ$ configuration which gives optimum results for $\varphi_i = 140^\circ$ and $\varphi_o = 0^\circ$. These parameters result in a phase shift $\Delta\phi = 2.0\pi$, as desired, a large output intensity and an intensity ratio $I_{MIN}/I_{MAX} = 0.54$. (Note that using a configuration with a $\Delta\phi$ significantly larger than 2π would reduce the usable range of $N_{\Delta\phi}$.) The actual phase shift $\Delta\phi$ as a function of $N_{\Delta\phi}$ for this configuration is shown in figure 7. The non-linearity is corrected for by the software.

5 Trap calibration and use

5.1 Active method: Oscillatory drag force

We use an oscillatory calibration technique, based on the drag force method, first demonstrated in [25]. However, here the trap is moved instead of the stage, and a precise positional calibration of

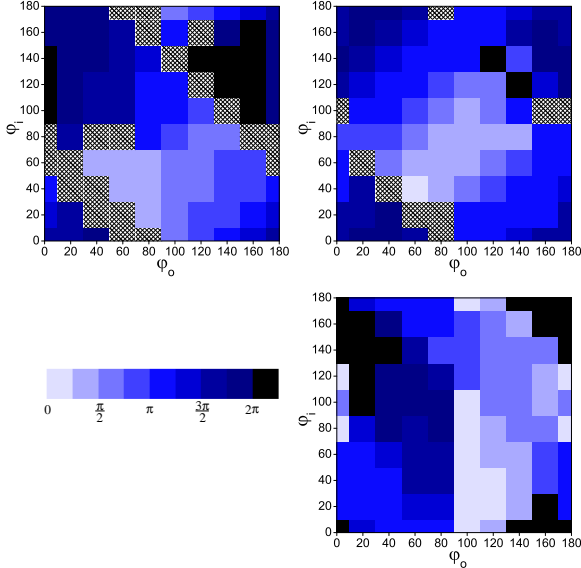


Figure 6: Maximum range of the actual phase shift $\Delta\phi$ as a function of input, φ_i , and output, φ_o , polarisation for different incident angles $\alpha = 22.5^\circ$ and 45° (top left, top right). In the lower right figure $\alpha = 45^\circ$ and $\lambda=633$ nm, in all other figures $\lambda=532$ nm. The cross-hatched areas represent configurations where the intensity of one of the fringe signals dropped to zero, and therefore the phase shift could not be measured.

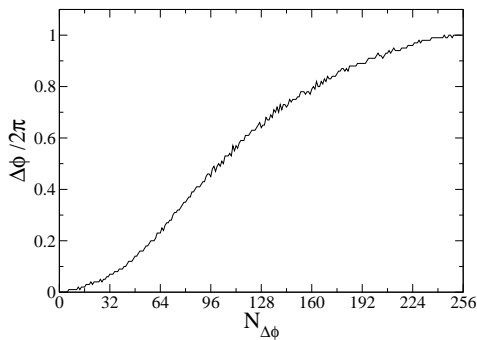


Figure 7: Phase shift $\Delta\phi$ as a function of $N_{\Delta\phi}$ for an incident angle of $\alpha = 22.5^\circ$ and an input and output polarisation of $\varphi_i=140^\circ$ and $\varphi_o=0^\circ$ respectively.

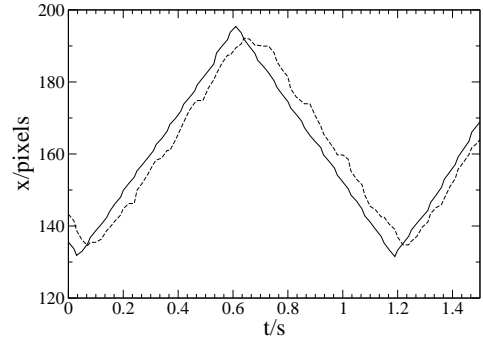


Figure 8: Position of the trap (solid line) and particle (dashed line) as a function of time t . Polystyrene-sulfonate particles with a radius of $2 \mu\text{m}$ in water at a temperature of 24° were used at a distance to the coverslip of more than $15 \mu\text{m}$, and a laser power of 11.1 mW. We determined a time lag $\Delta t = 31.7$ ms giving a trap stiffness $\kappa = 1.19 \times 10^{-3}$ pN/nm.

the stage is thus not required. A triangular wave signal is sent to the galvanometers. The reflection of the laser from the cover glass-water interface was tracked using one of the pattern matching algorithms in LabView. The time delay Δt_0 determined from a time correlation between the signal sent to the galvanometers and the signal recorded from the laser tracking provides the processing time of the hardware and software system. We subsequently trap a particle with radius R and perform the same procedure, but this time recording the particle position (fig 8). The time delay Δt_1 is determined from a time correlation between the galvanometer signal and particle signal. The time lag $\Delta t = \Delta t_1 - \Delta t_0$ is related to the trap stiffness $\kappa = 6\pi\eta R/\Delta t$. This is obtained by balancing the viscous drag due to particle velocity v in a viscous medium (viscosity η) $F_\eta = 6\pi\eta Rv$ and the trap force $F_{trap} = -\kappa\Delta x = -\kappa v\Delta t$. This assumes that the trap potential is harmonic, which is valid for $\Delta x < 0.55R$ (determined experimentally for 1064 nm wavelength optical tweezers [26]), and an individual particle in bulk.

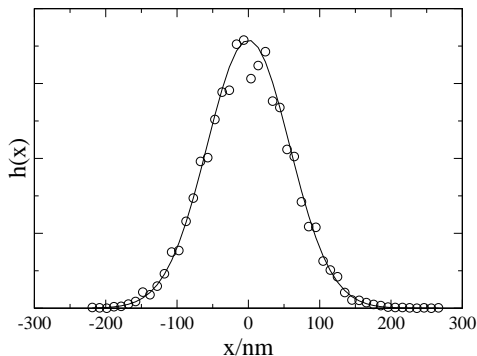


Figure 9: Histogram of particle positions $h(x)$, within the trap. The fitted gaussian has a variance $\sigma^2 = 3.35 \times 10^{-15} \text{ m}^2$, giving a trap stiffness $\kappa = 1.22 \times 10^{-3} \text{ pN/nm}$. The same sample and experimental conditions are used as in fig 8.

5.2 Passive method: Probability distribution

In this method, a particle or several particles are held in stationary traps and their positions in one dimension determined using video microscopy and particle tracking. We record the position x at 60 Hz for 250 seconds. This provides a histogram of the positions, $h(x)$, whose bin size was chosen to coincide with the accuracy of the particle tracking technique (fig 9). A gaussian is fitted to the histogram whose variance σ^2 is related to the trap stiffness via $\kappa = k_B T / \sigma^2$ [13]. We obtained consistent results with the two methods.

5.3 Dynamic particle arrays

With our optimised SLM we can generate arrays of traps (fig 10). The SLM allows us to trap particles in three dimensions. This represents an advantage over acousto-optic deflectors, with which it is possible to trap particles in more than one plane [14], but full control in 3d is not yet possible. Our set-up furthermore provides great flexibility in moving particles due to the combination of the SLM with the galvanometer-mounted mirrors. This combination allows for fast and smooth movements of the trap array. In contrast, translation of the traps using the SLM alone would be limited by the refresh rate of the SLM (for pre-calculated holograms) or

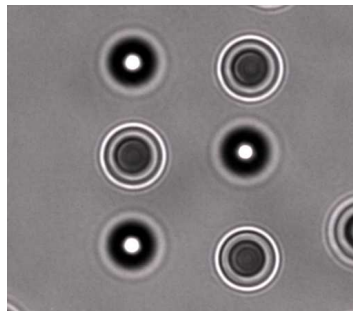


Figure 10: Image of six polystyrene particles with a diameter of $4 \mu\text{m}$, 3 trapped above and three trapped below the imaging plane.

the processing speed of the host computer (for real-time applications).

6 Conclusions

We have constructed optical tweezers which combine galvanometer-mounted mirrors and a spatial light modulator (SLM). We optimised the SLM with respect to its amplitude and phase shift which allows us to create complex arrays of traps in three dimensions. We can move the array in a smooth and fast way with the help of the galvanometer-mounted mirrors. It furthermore permits us to calibrate the traps using two methods, a drag force method and a probability distribution method. The trap strength measurements using both methods agree within experimental accuracy.

Acknowledgements

We thank Jörg Bewerunge for help with the alignment and optimisation, the group of Prof. M. Padgett (Glasgow) for sharing code to control the tweezers and Beate Moser for preparing the drawings. This work was funded by the Deutsche Forschungsgemeinschaft (DFG) Sonderforschungsbereich-Transregio 6, project C7, and the priority program SPP ‘Heterogeneous Nucleation and Microstructure Formation’. RDLH acknowledges the Marie-Curie Early Stage Training Network on ‘Biomimetic Systems’ (Contract MEST-CT-2004-504465) and the International Helmholtz Research School (IHRS) ‘BioSoft’.

References

- [1] Ashkin, A. *Phys Rev Lett* **24(4)**, 156 (1970).
- [2] Ashkin, A., Dziedzic, J. M., Bjorkholm, J. E., and Chu, S. *Opt Lett* **11(5)**, 288 (1986).
- [3] Molloy, J. E. and Padgett, M. J. *Contemp Phys* **43**, 241 (2002).
- [4] Grier, D. G. *Nature* **424(6950)**, 810 (2003).
- [5] Otto, O., Gutsche, C., Kremer, F., and Keyser, U. F. *Rev Sci Instrum* **79(2)**, 023710 (2008).
- [6] Bartlett, P. and Henderson, S. *J Phys: Condens Matter* **14(33)**, 7757 (2002).
- [7] Dufresne, E. R. and Grier, D. G. *Rev Sci Instrum* **69(5)**, 1974 (1998).
- [8] Reicherter, M., Haist, T., Wagemann, E. U., and Tiziani, H. J. *Opt Lett* **24(9)**, 608 (1999).
- [9] Liesener, J., Reicherter, M., Haist, T., and Tiziani, H. J. *Opt Commun* **185(1-3)**, 77 (2000).
- [10] Dufresne, E. R., Spalding, G. C., Dearing, M. T., Sheets, S. A., and Grier, D. G. *Rev Sci Instrum* **72(3)**, 1810 (2001).
- [11] Curtis, J. E., Koss, B. A., and Grier, D. G. *Opt Commun* **207(1-6)**, 169 (2002).
- [12] Sinclair, G., Jordan, P., Courtial, J., Padgett, M., Cooper, J., and Laczik, Z. *Opt Express* **12(22)**, 5475 (2004).
- [13] Simmons, R., Finer, J., Chu, S., and Spudich, J. *Biophys J* **70(4)**, 1813 (1996).
- [14] Vossen, D. L. J., van derHorst, A., Dogterom, M., and vanBlaaderen, A. *Rev Sci Instrum* **75(9)**, 2960 (2004).
- [15] Biancaniello, P. L. and Crocker, J. C. *Rev Sci Instrum* **77(11)**, 113702 (2006).
- [16] Neuman, K. C. and Block, S. M. *Rev Sci Instrum* **75(9)**, 2787 (2004).
- [17] Gutsche, C., Keyser, U. F., Kegler, K., Kremer, F., and Linse, P. *Phys Rev E* **76(3)**, 031403 (2007).
- [18] Ghislain, L. P., Switz, N. A., and Webb, W. W. *Rev Sci Instrum* **65(9)**, 2762 (1994).
- [19] Rohrbach, A. *Opt Express* **13(24)**, 9695 (2005).
- [20] Di Leonardo, R., Ianni, F., and Ruocco, G. *Opt Express* **15(4)**, 1913 (2007).
- [21] Michelson, A. A. and Morley, E. W. *Am J Sci* **34**, 333 (1887).
- [22] Zehnder, L. *Z Instrumentenkd* **11**, 275 (1891).
- [23] Mach, L. *Z Instrumentenkd* **12**, 89 (1892).
- [24] Martin-Badosa, E., Carnicer, A., Juvells, I., and Vallmitjana, S. *Meas Sci Technol* **8(7)**, 764 (1997).
- [25] Kuo, S. and Sheetz, M. *Science* **260(5105)**, 232 (1993).
- [26] Richardson, A. C., Reihani, S. N. S., and Oddershede, L. B. *Opt Express* **16(20)**, 15709 (2008).